Corrosion Science 52 (2010) 1610–1617

Contents lists available at ScienceDirect

Corrosion Science

journal homepage: www.elsevier.com/locate/corsci

Corrosion properties of friction–stir processed cast NiAl bronze

D.R. Ni [a], B.L. Xiao [a], Z.Y. Ma [a,*], Y.X. Qiao [b,c], Y.G. Zheng [b]

[a] Shenyang National Laboratory for Materials Science, Institute of Metal Research, Chinese Academy of Sciences, 72 Wenhua Road, Shenyang 110016, China
[b] State Key Laboratory for Corrosion and Protection, Institute of Metal Research, Chinese Academy of Sciences, 62 Wencui Road, Shenyang 110016, China
[c] Suzhou Nuclear Power Research Institute, 1788 Xihuan Roud, Suzhou 215004, China

ARTICLE INFO

Article history:
Received 17 July 2009
Accepted 11 February 2010
Available online 16 February 2010

Keywords:
A. NiAl bronze
A. Copper
B. Weight loss
B. Polarization
B. Friction–stir processing

ABSTRACT

Friction–stir processing (FSP) was adopted to modify the microstructure of a cast Cu–9Al–4.5Ni–4Fe NiAl bronze alloy (NAB). After FSP, the initial coarse microstructure of the cast NAB was transformed to a fine structure, and the porosity defects were eliminated. The microstructure modification changed the corrosion behavior of the NAB in a 3.5% NaCl solution. In a static immersion corrosion test, the FSP NAB exhibited significantly greater corrosion resistance compared to the cast counterpart. The polarization curve and electrochemical impedance spectroscopic (EIS) results indicated that the FSP NAB showed slightly lower electrochemical corrosion resistance.

1. Introduction

Due to the high mechanical properties and excellent erosion–corrosion resistance, nickel–aluminum bronzes (NAB) are extensively used for propulsion and seawater handling systems [1–6]. As a quaternary system, these alloys typically contain 9–12% Al with additions of up to 6% each of Fe and Ni. The addition of Ni and Fe into binary Cu–Al alloys extends the terminal fcc α-phase field and suppresses the formation of γ-phase that occurs in the Cu–Al alloys, Al_4Cu_9, which is deleterious to the corrosion resistance of the alloys due to the high Al content [1]. The cast NAB is mainly composed of coarse Widmanstätten α phase, nickel–iron–aluminum κ phases, and island martensite β′ phase, and the transformation phases and their precipitation sequence are complex [7–12]. Furthermore, the defect of shrinkage porosity is prone to appear in the cast alloys due to their poor casting properties, which is undoubtedly injurious to the mechanical and corrosion properties of components.

Although the NAB own good corrosion resistance, in order to further improve its erosion–corrosion performance the use of organic and metallic coatings has been investigated [13], which is also a cost-effective approach for recovering components that are worn or corroded. However, the coating approach can not enhance the mechanical properties, which could be achieved by the refinement of coarse cast structure and the elimination of porosity defects. So, a method which could improve both the mechanical and erosion–corrosion properties of the cast NAB is expected.

Friction–stir processing (FSP) is a multifunctional metal working technique developed based on the basic principles of friction–stir welding (FSW) [14–16]. This technique has been successfully employed to modify the microstructure of heterogeneous metallic materials [17], to produce surface composites [18,19], and to synthesize composites and intermetallic compounds [20,21]. An important function of FSP is to provide localized modification and control of microstructure in the near-surface region of castings without changing the shape of components, with the aim to repair defects and to refine and homogenize the coarse microstructures.

Previous investigations have showed that FSP refined the coarse microstructure of the cast NAB, healed the porosity defect, and homogenized the microstructure, thereby increasing the hardness, tensile properties, and fatigue strength [22–25]. Oh-ishi et al. [26–30] reported that the main characteristic of the stir zone (SZ) of the FSP NAB was inhomogeneous microstructures in various sub-regions, including Widmanstätten structure, equiaxed fine grain structure, and banded or lamellar structure. Similar results were also reported by other researchers [23,31]. More recently, our study further showed that the inhomogeneous microstructure was parameters dependent, and both the hardness and the tensile properties of the cast NAB were greatly improved by FSP [32].

FSP definitely refined and homogenized the microstructure of the cast NAB, however, at the same time, the change in the

Abbreviations: FSP, friction–stir processing; FSW, friction–stir welding; SZ, stir zone; AS, advancing side; RS, retreating side; NAB, NiAl bronze; OM, optical microscope; SEM, scanning electron microscope; SCE, saturated calomel reference electrode; EIS, electrochemical impedance spectroscopy; OCP, open circuit potential; NC, nanocrystallized; CG, coarse-grained; WL, Weight loss; WLR, weight loss rate.

* Corresponding author. Tel./fax: +86 24 83978908.
E-mail address: zyma@imr.ac.cn (Z.Y. Ma).

0010-938X/$ - see front matter © 2010 Elsevier Ltd. All rights reserved.
doi:10.1016/j.corsci.2010.02.026

microstructure undoubtedly produced a large volume fraction of intercrystalline defects such as the grain boundaries and dislocations. Considering the fact that the NAB is usually used in the corrosion environment, it is of practical importance to understand whether the FSP microstructure which enhances the mechanical properties of the NAB, has a detrimental effect on corrosion performance. In fact, previous investigations revealed that the FSW joints [33–36] and FSP materials [37–39] exhibited different corrosion behaviors compared to the base materials.

So far, investigations of the FSP NAB were mainly focused on the microstructure evolution with a small portion on the mechanical properties; however, the corrosion behavior of the FSP NAB has rarely been studied yet. Prevey et al. [25] investigated the electrochemical corrosion curves of the FSP NAB in both neutral and acidic 3.5% NaCl solution, and reported that FSP increased the corrosion resistance of the cast NAB. However, the corrosion behavior and mechanism were not discussed. In this study, the corrosion properties of FSP Cu–9Al–4.5Ni–4Fe in 3.5% NaCl solution was investigated and compared to those of the cast counterpart. The aim is to examine the effect of FSP on the corrosion properties of the NAB and understand the corrosion mechanism.

2. Experimental

2.1. Material

Commercial UNS C95800 NAB alloy (chemical composition in wt.%: Al 9.18, Ni 4.49, Fe: 4.06, Mn 1.03, and Cu balance) cast plates with dimension of 300 mm × 70 mm × 8 mm were subjected to FSP under a tool rotation rate of 1200 rpm and a traverse speed of 50 mm min^{-1} with a tool tilt angle of 3°. A nickel-based alloy tool with a concave shoulder 24 mm in diameter, and a threaded conical pin 8 mm in root diameter and 7 mm in length was used. Both the tool and the processed workpiece were subjected to blow over cooling during FSP. The microstructure of the cast and FSP samples were examined using optical microscopy (OM) after etching with solution of 5 g $FeCl_3$ + 2 ml HCl + 95 ml C_2H_5OH.

2.2. Static immersion corrosion

Static immersion samples were machined from the SZ with a dimension of 7 mm × 7 mm × 5 mm (Fig. 1) and were ground with 1000 SiC abrasive paper to provide a uniform surface finish. Prior to test, the samples were degreased in acetone and blow-dried, and weighed carefully. Fifteen samples were suspended by the thin threads, respectively, and immersed into a tank containing 10 L of a 3.5 wt.% NaCl solution at room temperature. The solution was prepared from distilled water and reagent grade chemicals. The corroded samples were taken out after 24, 48, 96, 192, and 384 h, respectively. The corroded samples were flushed with water and immersed in the solution of 500 ml HCl (density, 1.19) + 1000 ml H_2O for 2 min to clean off the corrosion products, then completely rinsed out using a toothbrush and flushed with water, and then immersed in alcohol and blow-dried, and finally weighed. The gravimetric measurements were made by using a Mettler XS105 Dualrange precision balance (with a range of 41/120 g and an accuracy of ±0.01/0.1 mg). The weight loss for each condition was obtained by averaging three results. For the purpose of comparison, the cast samples with the same size were tested under the same conditions. Corrosion surfaces were examined under an optical microscope (OM) and a scanning electron microscope (SEM), and furthermore, part of the corrosion specimens were mounted, polished, and examined under a SEM.

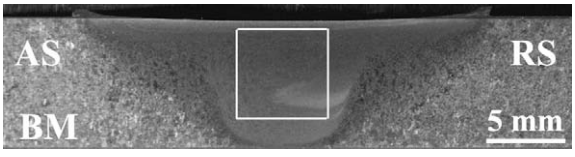

Fig. 1. Cross-sectional macrograph of FSP NAB sample.

2.3. Electrochemical measurements

Samples similar to those for the immersion corrosion were prepared with polished surface. The working area exposed to tested solution was 0.49 cm^2 and all other unexposed area was coated with epoxy resin. The test medium was 3.5% NaCl solution. The electrochemical measurements were performed with a standard three-electrode system in a 1.5 L glass cell at ambient temperature (22–25 °C) in open air without stirring, by using a model 2273 potentiostat/galvanostat which was controlled by M352 software provided by EG&G PAR company. A three-electrode cell setup consisting of a Pt counter electrode, a saturated calomel reference electrode (SCE) and a specimen as working electrode was employed, and all the potentials measured were referred to SCE. Prior to measurement, the working electrodes were immersed in the solution for at least 1 h to obtain a stable condition. Polarization curves were recorded at a sweep rate of 0.166 mV s^{-1}. Electrochemical impedance spectroscopic (EIS) experiments were carried out using a 20 mV perturbation from 20 kHz to 10 mHz. All of the measurements were repeated three times to ensure good reproducibility.

3. Results

3.1. Microstructure

Fig. 1 shows the optical cross-sectional macrograph of the FSP NAB. The microstructure of the cast sample was composed of coarse Widmanstätten α phase, coarse martensite β′ phase, fine κ phase particles, and casting porosities (Fig. 2). The light-etching phase with a size of ~150 μm was the α phase, whereas the dark-etching constituents were associated with the various β transformation products.

The FSP NAB was characterized by densified fine-grained structure and consisted of inhomogeneous microstructures: fine Widmanstätten primary α phase in the surface layer, banded primary α and β′ phases in the subsurface layer, equiaxed α and β′ phases with a size of less than 10 μm in the center, and streamlike α and β′ phases at the bottom; meanwhile, FSP alleviated the severe composition segregation in the cast NAB: the element Ni and Fe were uniformly distributed around equiaxed α particles after FSP [32]. The microstructure of the FSP NAB has been discussed in detail in our previous report [32], so it was not described here any more. The center region possessed most parts of the SZ, in which few α phase and partial κ phases transformed into the β phase during FSP, and most of the α phase converted into equiaxed grains due to the dynamic recrystallization resulting from severe deformation (Fig. 3). The FSP NAB showed much better mechanical properties than the cast counterpart (Table 1).

3.2. Static immersion corrosion

The weight loss rates of the cast and FSP NAB are showed in Fig. 4. Three important observations can be made. First, the cast NAB exhibited apparently higher weight loss rate than the FSP NAB during the test. Second, the weight loss rates of both the cast and FSP samples decreased with increasing the time. Third, the

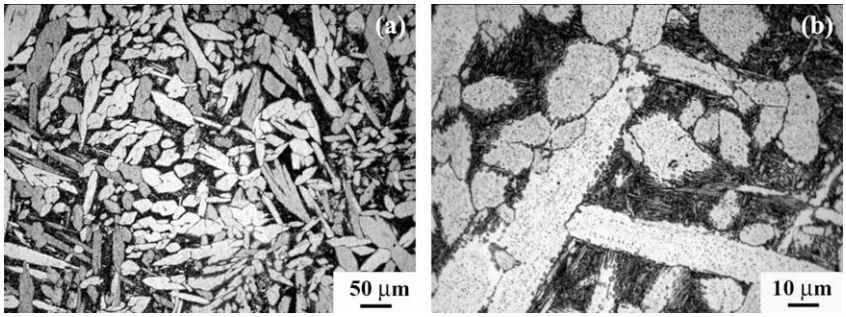

Fig. 2. Optical microstructure of cast NAB sample: (a) Widmanstätten morphology and porosities, (b) precipitates.

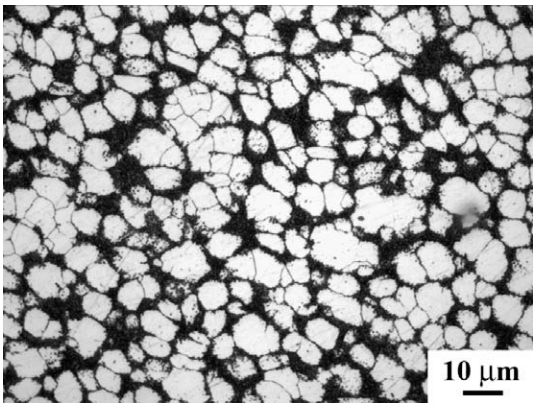

Fig. 3. Optical microstructure in the center of the stir zone of FSP NAB sample.

Table 1
Mechanical properties of cast and FSP NAB alloy.

Sample	YS (MPa)	UTS (MPa)	EL (%)	Hardness (Hv)
FSP-transverse	502 ± 21	838 ± 12	29 ± 1.5	210
FSP-longitudinal	469 ± 17	804 ± 15	28 ± 6.9	–
Cast	282 ± 2	645 ± 29	18 ± 6.6	175

Gauge dimension: 5 × 1.5 × 0.85 mm for FSP sample, 60 × 12 × 8 mm for cast sample.
Hardness: micro-vickers hardness tester, 5 kg for 15 s.

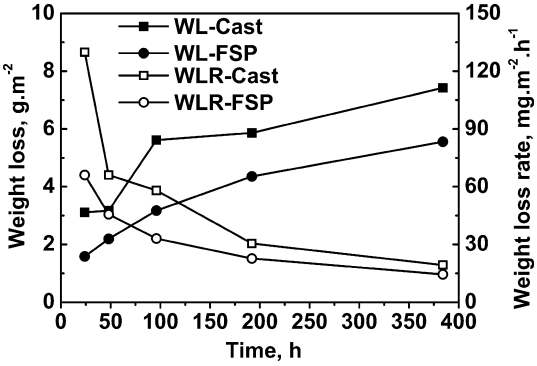

Fig. 4. Weight loss (WL) and weight loss rate (WLR) of cast and FSP NAB samples in 3.5% NaCl solution.

weight loss rates can be divided into two stages: higher rate before 192 h; lower rate after 192 h which tended to be steady.

Figs. 5–7 show the surfaces of post-corrosion samples. After 24 h, the cast sample exhibited very obvious corrosion, with white corrosion scars about 50 μm in size being distributed on the surface (Fig. 5a). Higher magnification revealed that the scars appeared at the κ-rich location (Fig. 5b). Meanwhile, some pores were found on the surface (Fig. 5c). By comparison, the FSP sample was slightly corroded, and only some small corrosion scars less than 10 μm in size scattered on the surface (Fig. 5d). After 192 h, the corrosion was particularly evident on both the cast and FSP samples (Fig. 6). For the cast sample, both the amount and the size of the scars apparently increased with some larger ones being ~100 μm in size (Fig. 6a). The FSP sample was covered with small scars (Fig. 6b). After 384 h, the corrosion increased further, and the initial surface of both the cast and FSP samples was corroded out and original grinding marks on the surface disappeared completely (Fig. 7).

Fig. 8 shows the backscattered electron image of the cross-section of the corroded samples after exposure to 3.5% NaCl solution for 384 h. For the cast sample, the surface was rough, and the κ phase-rich region was more seriously corroded than the α phase region (Fig. 8a). Furthermore, the shrinkage cavity was revealed below the surface and this accelerated the corrosion process (Fig. 8b and c). For the FSP sample, the surface was relatively even and no κ phase-rich regions and shrinkage cavity were observed (Fig. 8d).

3.3. Electrochemical corrosion

The electrochemical polarization behavior of the NAB in 3.5% NaCl solution is illustrated in Fig. 9. Both the cast and FSP samples exhibited similar polarization curves, indicating no significant difference in the polarization behavior between the two samples. Apparently, the cathodic process is the rate-controlling step for the whole corrosion process. The reaction that took place at the cathode was mainly the oxygen reduction reaction. At the applied potential range of −0.75 to −0.3 V_{SCE}, the cathodic curves were almost perpendicular to the horizontal axis, showing the feature of the limiting diffusion current density. This was mainly due to the limited diffusion of oxygen. From −0.3 V_{SCE} to the corrosion potential, the cathode reduction reaction rate decreased gradually as the corrosion potential in the positive direction shifted. The anodic part of the curves was in accordance with the Tafel feature. But at an applied potential of close to 0 $V_{SCE,}$ the current density of the two samples first decreased as the applied potential was increased, indicating the formation of possible poor surface film on the sample surface (considering the overly high current density), and then increased with the increase of the applied potential. The cast sample showed slightly higher corrosion potential and lower corrosion current density, consequently showing slightly better electrochemical corrosion resistance, than the FSP one.

In order to verify the electrochemical results of the aforementioned polarization curve, EIS measurements were also carried out. Nyquist plots for the NAB at free corrosion potential in the tested solution are presented in Fig. 10. The Nyquist plot

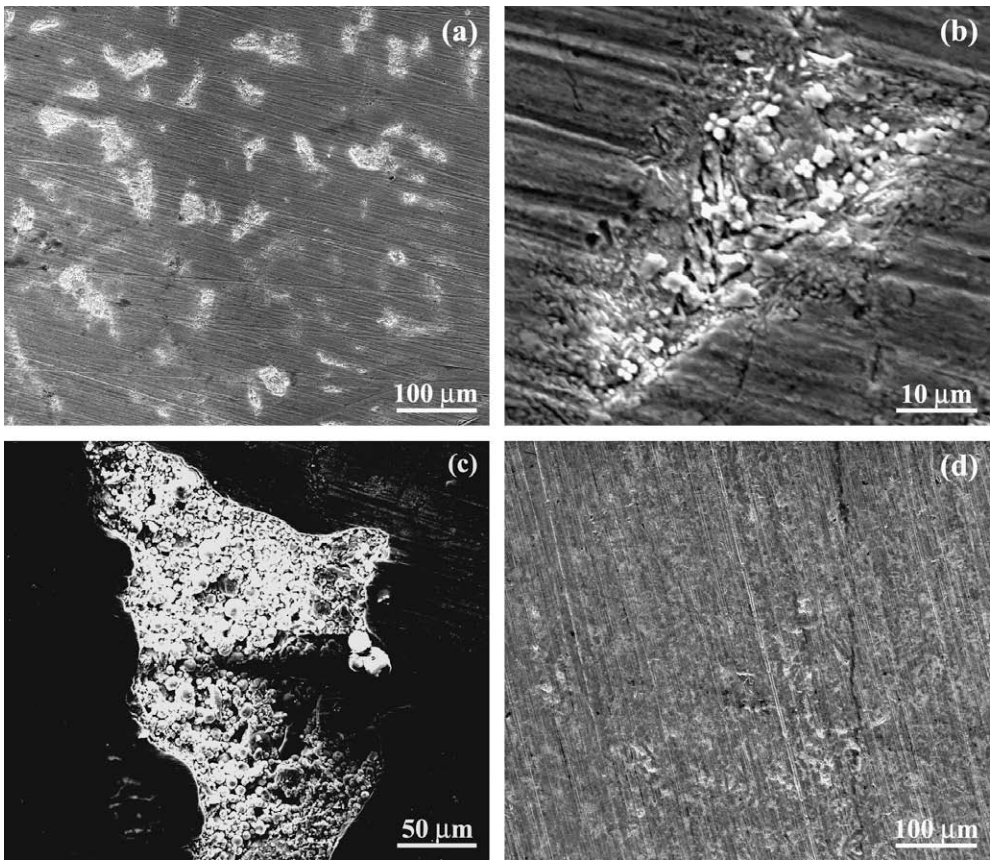

Fig. 5. SEM micrographs of NAB sample surfaces after exposure to 3.5% NaCl solution for 24 h: (a) cast NAB; (b) higher magnification showing a typical corrosion scar in (a); (c) a cast pore in cast NAB; (d) FSP NAB.

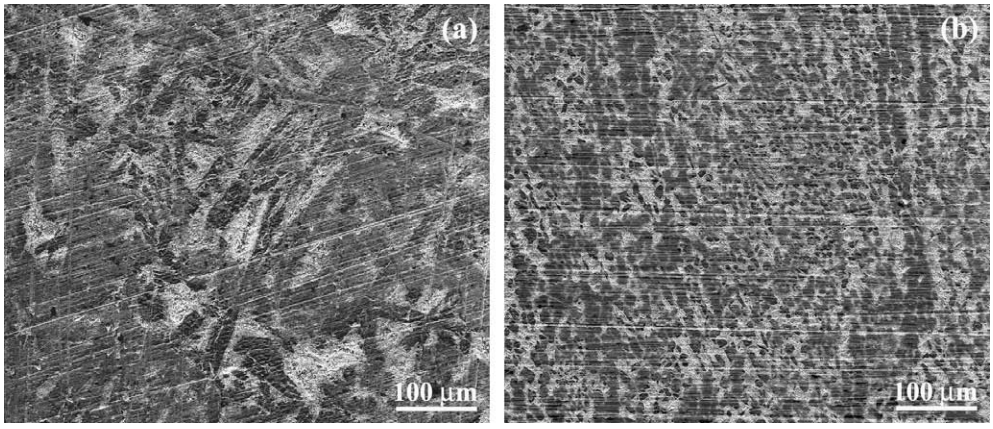

Fig. 6. SEM micrographs of NAB sample surfaces after exposure to 3.5% NaCl solution for 192 h: (a) cast NAB; (b) FSP NAB.

of both the cast and FSP samples consisted of two parts: high frequency capacitance arc, and low frequency impedance arc with Warburg feature. The high frequency capacitance arc reveals the characteristics of surface film at the interface of the matrix and the solution. The capacitive arc for the cast sample was broader than that for the FSP sample, indicating that the corrosion rate of the FSP sample was higher than that of the cast sample. This is contrary to the static immersion results and will be discussed later. It can be also seen from the Nyquist plot that the boundary between the high frequency impedance and low frequency Warburg arc for the cast sample was not as distinct as that for the FSP one.

4. Discussion

4.1. Microstructural characteristics

The cast NAB is characterized by its complex phases and phase formation sequence [12,26]. Below 1030 °C the primary α phase with a Widmanstätten morphology forms in the β phase; at about 930 °C, globular κ_{ii} phase begins to nucleate, which is nominally Fe_3Al; at about 860 °C, fine κ_{iv} precipitates begin to form, which are also nominally Fe_3Al; at about 800 °C, the retaining β decomposes by a eutectoid reaction that results in the formation of a nickel-rich κ_{iii} phase, which has a lamellar morphology. However,

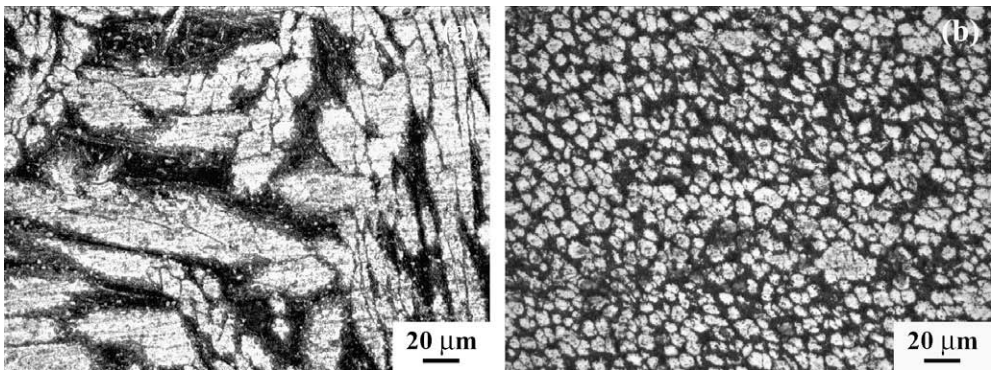

Fig. 7. Optical micrograph of NAB sample surfaces after exposure to 3.5% NaCl solution for 384 h: (a) cast NAB; (b) FSP NAB.

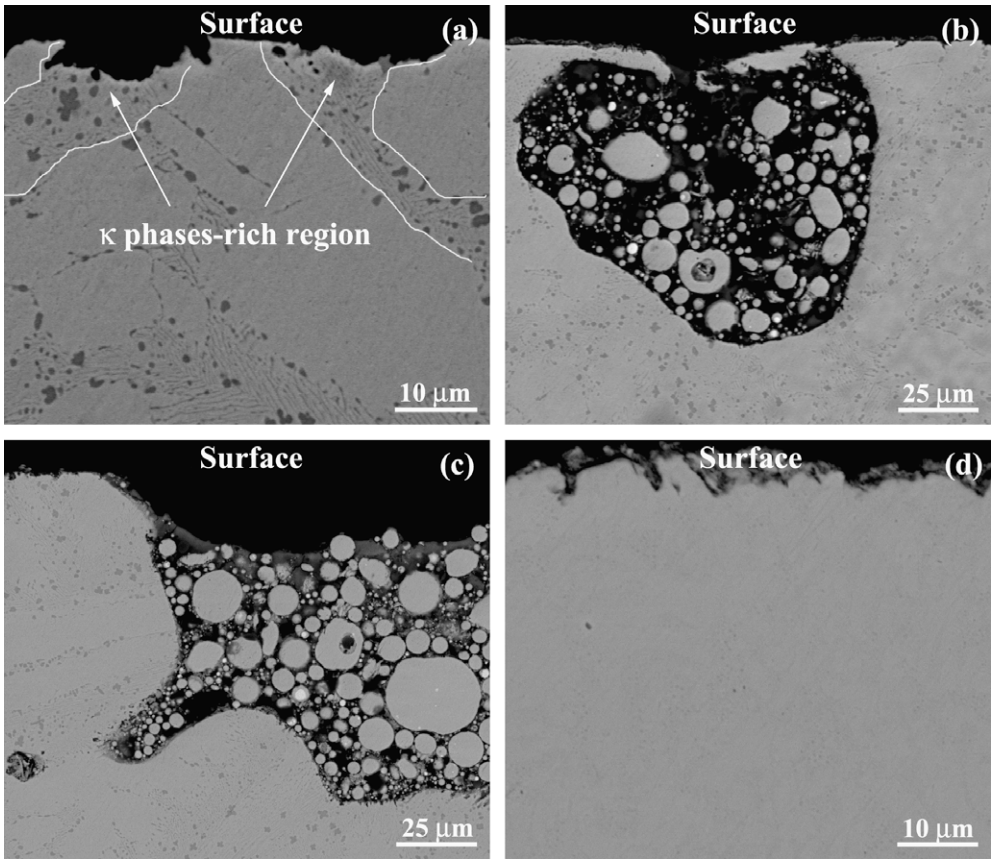

Fig. 8. Backscattered electron images of cross-sectional NAB samples after exposure to 3.5% NaCl solution for 384 h: (a) cast NAB; (b) and (c) pores in cast NAB; (d) FSP NAB.

the equilibrium cooling rates of the NAB is quite slow, about on the order of 10^{-3} K s^{-1}, which is difficult to realize in practice. Consequently, the transformation products of the NAB, especially those produced in thick sections retains some β phases which have no time to decompose. These "retained β" owns a martensitic structure and is termed β′. Thus, at room temperature, the cast NAB alloy is mainly composed of coarse Widmanstätten α phase, particle κ phases, and island martensite β′ phase. At the same time, the slow cooling rate is likely to result in increased grain size, microsegregation of alloying elements, larger κ phase precipitates, and micro- and macro-defects, particularly shrinkage porosity defects.

FSP refined the microstructure of the cast NAB, resulting in the significant breakup and decomposition of coarse Widmanstätten α phase and κ phases, the elimination of casting porosities, and the uniform distribution of phases. Oh-ishi et al. [26] reported that FSP partially dissolved α, κ_{ii}, κ_{iii}, and κ_{iv} phases into the β, and furthermore, the severe deformation and heating during FSP also resulted in recovery and recrystallization in the deformed α matrix as well as spheroidization of retaining lamellar κ_{iii}. The fine and equiaxed α grain was the predominant constituent of the microstructure in the FSP NAB. The effect of dissolving second phase by FSP was also found in magnesium alloys. Feng and Ma [40] reported that in situ two pass FSP resulted in the dissolution of most $Mg_{17}Al_{12}$ in the cast AZ91D magnesium alloy, which is similar to the effect of solution heat treatment at high temperature for a long time. In addition, FSP alleviated the severe composition segregation in the cast NAB [32], and this may affect the corrosion resistance greatly.

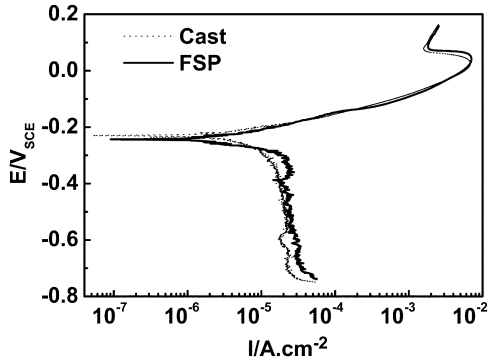

Fig. 9. Potentiodynamic polarization curves of NAB samples in aerated 3.5% NaCl solution.

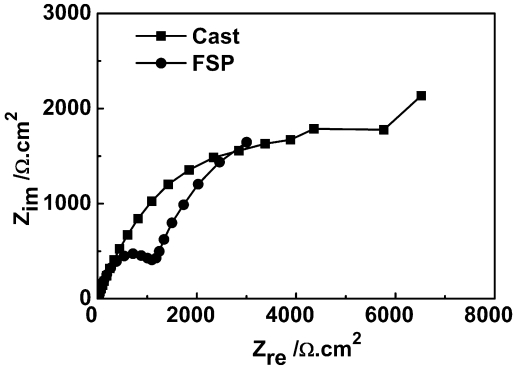

Fig. 10. Nyquist plots of NAB samples in 3.5% NaCl solution.

4.2. Static immersion corrosion

The corrosion behavior of the cast NAB in seawater has been well documented previously [1–6,41–44]. Kear et al. [45] reviewed the corrosion of copper in chloride medium, and pointed out that the corrosion was complicated by the formation of surface films. By analogy with copper, it is well established [5,6] that the major electrode processes of the NAB were anodic dissolution of copper to form the cuprous dichloride anion simplified as (1) together with oxygen reduction as the primary cathodic process (2):

$$Cu + 2Cl^- - e^- \rightarrow CuCl_2^- \quad (1)$$

$$O_2 + 2H_2O + 4e^- \rightarrow 4OH^- \quad (2)$$

And cuprous oxides (mainly Cu_2O) were formed by a dissolution/precipitation process [41], as following:

$$2CuCl_2^- + 2OH^- \rightarrow Cu_2O + H_2O + 4Cl^- \quad (3)$$

The addition of Al increases the corrosion resistance of copper in seawater due to the formation of a film of hydrated Al oxide/hydroxide, and this layer is formed by the complexation of Al by chloride, followed by hydrolysis to produce an Al hydroxide layer [41]:

$$Al + 4Cl^- \rightarrow AlCl_4^- + 3e^- \quad (4)$$

$$AlCl4^- + 3H_2O \rightarrow Al(OH)_3 + 3H^+ + 4Cl^- \quad (5)$$

Schüssler et al. [42,43] attributed the good corrosion resistance of the NAB to a protective oxide layer containing both Al and Cu oxides (mainly Cu_2O and Al_2O_3). The oxide layer was Al-rich in regions adjacent to the base metal and Cu-richer in the outer regions. The corrosion layers acted as a barrier and hampered the ionic transport across the corrosion product, especially the sustainable protective layer of alumina, which built up quickly on the alloy surface.

Wharton et al. [44] studied the corrosion characteristics of cast, wrought, and heat-treated NAB alloys in seawater using short term electrochemical techniques, impingement studies and longer term immersion trials. The wrought NAB showed little evidence of the β and κ_{iii} phases. A proper heat treatment resulted in the minimization or elimination of the more corrodible β-phase and an increased density of fine κ phase precipitates in the α-phase. The results showed that the metallurgical composition, history, and surface roughness affected the corrosion rate.

Furthermore, Wharton et al. [41] studied the crevice corrosion behavior of the NAB. Their results showed that the crevice corrosion was initially confined to the eutectoid regions with a slight attack of the Cu-rich α-phase within the $\alpha + \kappa_{iii}$ eutectoid. The continuous nature of the κ_{iii} phase made it vulnerable with an 80 μm depth of attack after only the first month. Although the eutectoidal α phase was preferentially attacked, the α-grains showed very little attack. This was attributed to the presence of a greater proportion of cathodic phase κ_{iii} in the eutectoid regions.

In the present paper, for the cast NAB, the corrosion of the Cu-rich α phase within the $\alpha + \kappa_{iii}$ eutectoid was apparent for the long term immersion corrosion, which was similar to the result of Wharton et al. [41]. By contrast, the corrosion of the FSP NAB was slight. The increase in the static immersion corrosion resistance of the FSP NAB is attributed to following factors.

First, the coarse microstructure of the NAB had a lower corrosion resistance than the finer counterpart. Ferrara and Caton [2] reported that the depth of attack in the cast NAB was strongly influenced by the size and distribution of microconstituents, and the coarser microstructures resulted in a deeper attack. The present result is in agreement with Ferraran and Caton's result. The coarse microstructure resulted in the segregation of elements especially in the grain boundaries and this could provide the corrosion path for the solution of preferentially corroded phases. FSP resulted in the breakup/decomposition of the coarse phases and the homogenization of elements. This greatly eliminated the corrosion path, thereby enhancing the corrosion resistance.

Second, the cast porosities in the cast sample provided shortcuts for corrosion. On the one hand, these regions showed much lower corrosion resistance than the densified regions (Fig. 8b). On the other hand, the porosities increased the area between the sample and the corrosion solution (Fig. 8c), and this further accelerated the corrosion process. However, FSP eliminated the porosities, and therefore increased the corrosion resistance effectively.

Third, the κ phases (FeAl, Fe_3Al, NiAl, Ni_3Al) were coarse and exhibited an inhomogeneous distribution in the cast NAB, and this promoted the corrosion. FSP not only changed the morphology of the κ phases but also alleviated the segregation, thus increasing the corrosion resistance. Surekha et al. [37,38] reported that FSP increased the salt spray corrosion, immersion corrosion, and electrochemical corrosion resistances of AA 2219-T87 alloy in NaCl solution. The corrosion resistance increased with the increase in the number of the FSP pass and the rotation speed. The increased corrosion resistance was attributed to the dissolution of $CuAl_2$ particles, which reduced the number of sites available for galvanic coupling. The salt spray and immersion results of Surekha et al. were in agreement with our results, whereas the electrochemical result was not and this will be discussed later.

The weight loss rates of both cast and FSP samples decreased as the exposure time was increased, which resulted from the formation of a protective oxide layer on the sample surface, as mentioned above [5,6,41–45]. The corrosion layers acted as a barrier and hampered the ionic transport across the corrosion products, and thereby decreasing the corrosion rate.

4.3. Electrochemical corrosion

The electrochemical test results showed that the FSP sample exhibited slightly lower electrochemical corrosion resistance than the cast sample. This is basically consistent to the results of Prevey et al. [25]. They reported that there was no significant difference between the electrochemical polarization curves of the FSP and cast NAB in both the neutral and acidic 3.5% NaCl solution. FSP only very slightly increased the open circuit potential (OCP) of the cast NAB in the neutral solution, from −0.265 to −0.257 V_{SCE}. However, in the acidic solution the OCP of the cast sample decreased substantially, while the FSP NAB showed little change in the OCP (−0.350 and −0.262 V_{SCE}, respectively).

FSP slightly decreased the electrochemical corrosion resistance of the cast NAB, and this should be ascribed to two respects. First, FSP resulted in severe plastic deformation and therefore generated residual stress in the sample. It was reported [25] that residual stress exceeding +200 MPa and −200 MPa presented below the surface of the FSP NAB in the directions parallel and perpendicular to the FSP path, respectively. According to the Nernst equation, the Gibbs free energy increases and the electric potential decreases for a stressed sample, therefore its electrochemical corrosion resistance decreased. Lynch et al. [39] reported that FSP generated residual stress as high as +159 MPa in the SZ of a high-damping Mn–Cu alloy which was used for marine propellers. The FSP sample without stress relieving was corroded to similar depth as the cast NAB in seawater, and severe cracking and exfoliation occurred in the FSP sample. In contrast, the depth of the dealloyed regions for the FSP sample with stress-relieving by heat treatment was much less than that for the cast sample. They pointed out that the inferior corrosion resistance of the FSP sample without stress relieving compared to the cast counterpart was associated with microcracking and exfoliation driven by high residual stresses, and the better corrosion resistance of stress-relieved FSP material resulted from the refined structure.

Second, the finer microstructure would degrade electrochemical corrosion resistance. These phenomena have been early reported in nanocrystallized (NC) materials, such as Ni [46] and Ni–P [47] in sulfuric acid solutions, $Cu_{90}Ni_{10}$ alloy in neutral chloride solutions [48], and Co–Cu alloys in alkaline solutions [49]. Recently, Li and Oguzie et al. [50] reported that the surface nanograined microstructure in low-carbon steel accelerated the corrosion rate in the acidic environment, and the corrosion rate increased with the decrease of the grain size [51], and the bulk NC ingot iron also showed a lower corrosion resistance [52]. The reason was attributed to the increased number of the active sites caused by surface nanocrystallizing. Wang et al. [53] reported that in HCl or H_2SO_4 solutions, NC Co coating exhibited higher corrosion rate than coarse-grained (CG) Co coating. They considered that high grain boundary density in NC Co could provide high-density of active sites for preferential attack.

As the grain size was reduced, the area of the grain boundaries increased. On the one hand, the amount of atoms that participated in the reaction increases, resulting in a faster corrosion rate. On the other hand, the atoms on the grain boundaries had higher energy, and it was easy to take part in electrochemical reaction. Consequently, the FSP sample exhibited a lower electrochemical corrosion resistance. In fact, the corrosion performance is sensitive to both the nature of the metal system and the environment. The microstructure with finer grain size can also show an improved corrosion resistance, and this has been proved by many studies. For example, Wang et al. [53] reported that the NC Co coating exhibited improved corrosion resistance in NaOH or NaCl solutions, because the higher grain boundary density was apt to lead to the formation of a stable and protective passive film quickly and this decreased the corrosion rate.

The electrochemical test results in this study were in agreement with that of Kear et al. [5,6]. In their study, at potentials close to Ecorr, the short-term anodic polarization behavior of freshly polished BS CA104 NAB in dilute chloride media was analogous to copper where the reaction rate was controlled by a combination of both charge and mass transfer. Irreversible oxygen reduction was the primary electrochemical reaction close to the corrosion potential and hydrogen evolution was only significant at very large negative values of polarization from the corrosion potential (−0.7 to −0.8 V_{SCE}).

It is noticed that the FSP NAB exhibited higher corrosion resistance than the cast counterpart in the immersion corrosion test, and the situation was reversed in the electrochemical corrosion test. This phenomenon could be tentatively explained as below. The immersion corrosion test reflected the corrosion resistance of a sample over a long period of time, where the localized corrosion played a very important role. FSP presents a beneficial effect to the corrosion resistance of the cast NAB because FSP refined the coarse microstructure of the NAB, healed the porosity defect, and homogenized the microstructure. However, the electrochemical corrosion test showed the corrosion resistance of a sample over a short period of time, where the mechanical effects, such as the increase of inner stress, dislocations and the Gibbs free energy, had more effects on the corrosion resistance, which was consistent with the results reported by Liu et al. [54]. During the electrochemical test, especially the EIS test, the plots reflected only the surface layer of the sample in the short test periods (about 10 min during EIS test), and the relatively higher inner stress and Gibbs free energy induced by FSP led to the relatively lower corrosion resistance of the FSP sample compared to that of the cast sample. More electrochemical measurements after different immersion tests within the entire 384 h should be helpful for verifying the above explanation and will be considered in our future study.

5. Conclusions

1. The FSP sample showed much lower corrosion rate in the static immersion corrosion condition than the cast sample due to the optimization of the microstructure such as the refinement of grain size, elimination of casting porosities, and alleviation of the κ phase segregation. The weight loss rate of both the cast and FSP samples decreased as the corrosion time increased at the first stage, and then gradually reached a steady level.
2. Both the FSP and cast samples showed similar polarization curves. The FSP sample showed slightly lower corrosion potential and a little bit higher corrosion current density. The Nyquist diagram of both the FSP and cast samples consisted of two parts: a high frequency capacitance arc and a low frequency impedance arc with the Warburg feature. The capacitive arc of the cast sample was broader than that of the FSP sample, indicating that the corrosion rate of the FSP NAB was higher than that of the cast NAB. The slightly lower electrochemical corrosion resistance of the FSP sample was ascribed to the existence of residual stress, increased dislocations and Gibbs free energy.

Acknowledgements

This work was supported by the National Outstanding Young Scientist Foundation under Grant No. 50525103, the National Basic Research Program of China under Grant No. 2006CB605205, the National High-tech Research Program under Grant No. 2006AA03Z111, and the Hundred Talents Program of Chinese Academy of Sciences.

References

[1] E.A. Culpan, G. Rose, Corrosion behavior of cast nickel aluminium bronze in sea water, Br. Corros. J. 14 (1979) 160–166.
[2] R.J. Ferrara, T.E. Caton, Review of de-alloy of cast-aluminum bronze and nickel–aluminum bronze alloys in sea-water service, Mater. Perform. 21 (1982) 30–34.
[3] G.W. Lorimer, F. Hasan, J. Iqbal, N. Ridley, Observation of microstructure and corrosion behavior of some aluminium bronzes, Br. Corros. J. 21 (1986) 244–248.
[4] C.H. Tang, F.T. Cheng, H.C. Man, Effect of laser surface melting on the corrosion and cavitation erosion behaviors of a manganese–nickel–aluminium bronze, Mater. Sci. Eng. A 373 (2004) 195–203.
[5] G. Kear, B.D. Barker, K. Stokes, F.C. Walsh, Flow influence electrochemical corrosion of nickel aluminium bronze – part I. Cathodic polarization, J. Appl. Electrochem. 34 (2004) 1235–1240.
[6] G. Kear, B.D. Barker, K. Stokes, F.C. Walsh, Flow influence electrochemical corrosion of nickel aluminium bronze – part II. Anodic polarization and derivation of the mixed potential, J. Appl. Electrochem. 34 (2004) 1241–1248.
[7] E.A. Culpan, G. Rose, Microstructural characterization of cast nickel aluminium bronze, J. Mater. Sci. 13 (1978) 1647–1657.
[8] M. Sahoo, Structure and Mechanical properties of slow-cooled nickel–aluminum bronze alloy C95800, Trans. AFS 90 (1982) 913–926.
[9] A. Jahanafrooz, F. Hasan, G.W. Lorimer, N. Ridley, Microstructural development in complex nickel–aluminum bronzes, Metall. Trans. A 14A (1983) 1951–1956.
[10] E.A. Feest, I.A. Cook, Pre-primary phase formation in solidification of nickel–aluminium bronze, Met. Technol. 10 (1983) 121–124.
[11] F. Hasan, J. Iqbal, N. Ridley, Microstructure of as-cast aluminium bronze containing iron, Mater. Sci. Technol. 1 (1985) 312–315.
[12] F. Hasan, A. Jahanafrooz, G.W. Lorimer, N. Ridley, The morphology, crystallography, and chemistry of phases in as-cast nickel–aluminum bronze, Metall. Trans. A 13A (1982) 1337–1345.
[13] R.C. Barik, J.A. Wharton, R.J.K. Wood, K.S. Tan, K.R. Stokes, Erosion and erosion–corrosion performance of cast and thermally sprayed nickel–aluminium bronze, Wear 259 (2005) 230–242.
[14] R.S. Mishra, Z.Y. Ma, Friction–stir welding and processing, Mater. Sci. Eng. R 50 (2005) 1–78.
[15] R. Nandan, T. DebRoy, H.K.D.H. Bhadeshia, Recent advances in friction–stir welding-Process, weldment structure and properties, Prog. Mater. Sci. 53 (2008) 980–1023.
[16] P.L. Threadgill, A.J. Leonard, H.R. Shercliff, P.J. Withers, Friction–stir welding of aluminium alloys, Int. Mater. R. 54 (2009) 49–93.
[17] P.B. Berbon, W.H. Bingel, R.S. Mishra, C.C. Bampton, M.W. Mahoney, Friction–stir processing: a tool to homogenize nanocomposite aluminum alloys, Scripta Mater. 44 (2001) 61–66.
[18] R.S. Mishra, Z.Y. Ma, I. Charit, Friction–stir processing: a novel technique for fabrication of surface composite, Mater. Sci. Eng. A 341 (2002) 307–310.
[19] A. Shafiei-Zarghani, S.F. Kashani-Bozorg, A. Zarei-Hanzaki, Microstructures and mechanical properties of Al/Al_2O_3 surface nano-composite layer produced by friction–stir processing, Mater. Sci. Eng. A 500 (2009) 84–91.
[20] C.J. Hsu, C.Y. Chang, P.W. Kao, N.J. Ho, C.P. Chang, $Al–Al_3Ti$ nanocomposites produced in situ by friction–stir processing, Acta Mater. 54 (2006) 5241–5249.
[21] C.H. Chuang, J.C. Huang, P.J. Hsieh, Using friction–stir processing to fabricate MgAlZn intermetallic alloys, Scripta Mater. 53 (2005) 1455–1460.
[22] W.A. Palko, R.S. Fielder, P.F. Young, Investigation of the use of friction–stir processing to repair and locally enhance the properties of large NiAl bronze propellers, Mater. Sci. Forum 426–432 (2003) 2909–2914.
[23] M.W. Mahoney, W.H. Bingel, S.R. Sharma, R.S. Mishra, Microstructure modification and resultant properties of friction–stir processed cast NiAl bronze, Mater. Sci. Forum 426–432 (2003) 2843–2848.
[24] C.B. Fuller, M.W. Mahoney, W.H. Bingel, M. Calabrese, B. London, Tensile and fatigue properties of friction–stir processed NiAl bronze, Mater. Sci. Forum 539–543 (2007) 3751–3756.
[25] P.S. Prevey, D.J. Hornbach, D.N. Jayaraman, Controlled plasticity burnishing to improve the performance of friction–stir processed Ni–Al bronze, Mater. Sci. Forum 539–543 (2007) 3807–3813.
[26] K. Oh-ishi, T.R. McNelley, Microstructural modification of as-cast NiAl bronze by friction–stir processing, Metall. Mater. Trans. A 35A (2004) 2951–2961.
[27] K. Oh-ishi, A.M. Cuevas, D.L. Swisher, T.R. McNelley, The influence of friction–stir processing on microstructure and properties of a cast nickel aluminum bronze material, Mater. Sci. Forum 426–432 (2003) 2885–2890.
[28] K. Oh-ishi, T.R. McNelley, The influence of friction–stir processing parameters on microstructure of as-cast NiAl bronze, Metall. Mater. Trans. A 36A (2005) 1575–1585.
[29] K. Oh-ishi, A.P. Zhilyaev, T.R. McNelley, A microtexture investigation of recrystallization during friction–stir processing of as-cast NiAl bronze, Metall. Mater. Trans. A 37A (2006) 2239–2251.
[30] T.R. McNelley, K. Oh-ishi, A.P. Zhilyaev, Microstructure evolution and microstructure–property relationships in friction–stir processing of NiAl bronze, Mater. Sci. Forum 539–543 (2007) 3745–3750.
[31] M.D. Fuller, S. Swaminathan, A.P. Zhilyaev, T.R. McNelley, Microstructural transformations and mechanical properties of cast NiAl bronze: effects of fusion welding and friction–stir processing, Mater. Sci. Eng. A 463 (2007) 128–137.
[32] D.R. Ni, P. Xue, D. Wang, B.L. Xiao, Z.Y. Ma, Inhomogeneous microstructure and mechanical properties of friction–stir processed NiAl bronze, Mater. Sci. Eng. A 524 (2009) 119–128.
[33] D.A. Wadeson, X. Zhou, G.E. Thompson, P. Skeldon, L. Djapic Oosterkamp, G. Scamans, Corrosion behaviour of friction–stir welded AA7108 T79 aluminium alloy, Corros. Sci. 48 (2006) 887–897.
[34] Y.H. Jang, S.S. Kim, C.D. Yim, C.G. Lee, S.J. Kim, Corrosion behaviour of friction–stir welded AZ31B Mg in 3.5%NaCl solution, Corros. Eng. Sci. Tech. 42 (2007) 119–122.
[35] O. Hatamleh, P.M. Singh, H. Garmestani, Corrosion susceptibility of peened friction–stir welded 7075 aluminum alloy joints, Corros. Sci. 51 (2009) 135–143.
[36] R.C. Zeng, J. Chen, W. Dietzel, R. Zettler, J.F.D. Santos, M.L. Nascimento, K.U. Kainer, Corrosion of friction stir welded magnesium alloy AM50, Corros. Sci. 51 (2009) 1738–1746.
[37] K. Surekha, B.S. Murty, K. Prasad Rao, Microstructural characterization and corrosion behavior of multipass friction–stir processed AA2219 aluminium alloy, Surf. Coat. Tech. 202 (2008) 4057–4068.
[38] K. Surekha, B.S. Murty, K. Prasad Rao, Effect of processing parameters on the corrosion behaviour of friction–stir processed AA 2219 aluminum alloy, Solid State Sci. 11 (2009) 907–917.
[39] S.P. Lynch, D.P. Edwards, A. Majumdar, S. Moutsos, M.W. Mahoney, Friction–stir processing of a high-damping Mn–Cu alloy used for marine propellers, Mater. Sci. Forum 426–4 (2003) 2903–2908.
[40] A.H. Feng, Z.Y. Ma, Enhanced mechanical properties of Mg–Al–Zn alloy via friction–stir processing, Scripta Mater. 56 (2007) 397–400.
[41] J.A. Wharton, K.R. Stokes, The influence of nickel–aluminium bronze microstructure and crevice solution on the initiation of crevice corrosion, Electrochim. Acta 53 (2008) 2463–2473.
[42] A. Schüssler, H.E. Exner, The corrosion of nickel–aluminum bronzes in seawater – I. Protective layer formation and the passivation mechanism, Corros. Sci. 34 (1993) 1793–1802.
[43] A. Schüssler, H.E. Exner, The corrosion of nickel–aluminum bronzes in seawater – II. The corrosion mechanism in the presence of sulphide pollution, Corros. Sci. 34 (1993) 1793–1802.
[44] J.A. Wharton, R.C. Barik, G. Kear, R.J.K. Wood, K.R. Stokes, F.C. Walsh, The corrosion of nickel–aluminium bronze in seawater, Corros. Sci. 47 (2005) 3336–3367.
[45] G. Kear, B.D. Barker, F.C. Walsh, Electrochemical corrosion of unalloyed copper in chloride media – a critical review, Corros. Sci. 46 (2004) 109–135.
[46] R. Rofagha, R. Langer, A.M. El-Sherik, U. Erb, G. Palumbo, K.T. Aust, The corrosion behavior of nanocrystalline nickel, Scripta Metal. Mater. 25 (1991) 2867–2872.
[47] R. Rofagha, U. Erb, D. Ostrander, G. Palumbo, K.T. Aust, The effects of grain size and phosphorus on the corrosion of nanocrystalline Ni–P alloys, Nanostruct. Mater. 2 (1993) 1–10.
[48] A. Barbucci, G. Farnè, P. Matteazzi, R. Riccieri, G. Cerisola, Corrosion behaviour of nanocrystalline $Cu_{90}Ni_{10}$ alloy in neutral solution containing chlorides, Corros. Sci. 41 (1999) 463–475.
[49] V.M. López-Hirata, E.M. Arce-Estrada, Characterization of Co–Cu mechanical alloys by linear sweep voltammetry, Electrochim. Acta 42 (1997) 61–65.
[50] E.E. Oguzie, Y. Li, F.H. Wang, Effect of surface nanocrystallization on corrosion and corrosion inhibition of low carbon steel: synergistic effect of methionine and iodide ion, Electrochim. Acta 52 (2007) 6988–6996.
[51] Y. Li, F.H. Wang, G. Liu, Grain size effect on the electrochemical corrosion behavior of surface nanocrystallized low-carbon steel, Corrosion 60 (2004) 891–896.
[52] E.E. Oguzie, S.G. Wang, Y. Li, F.H. Wang, Corrosion and corrosion inhibition characteristics of bulk nanocrystalline ingot iron in sulphuric acid, J. Solid State Electrochem. 12 (2008) 721–728.
[53] L.P. Wang, Y.M. Lin, Z.X. Zeng, W.M. Liu, Q.J. Xue, L.T. Hu, J.Y. Zhang, Electrochemical corrosion behavior of nanocrystalline Co coatings explained by higher grain boundary density, Electrochim. Acta 52 (2007) 4342–4350.
[54] X.F. Liu, J. Zhan, Q.J. Liu, The influence of tensile stress on electrochemical noise from aluminum alloy in chloride media, Corros. Sci. 51 (2009) 1460–1466.